Calibrating TSA with integrated DIC: Application to fatigue cracks

Juliette Gamot, Thibaut Lasserre, Louis Richard, Jan Neggers, Nicolas Swiergiel, François Hild

Calibrating TSA with integrated DIC: Application to fatigue cracks

**Juliette Gamot,[1] Thibaut Lasserre,[1] Louis Richard,[1]
Jan Neggers,[2] Nicolas Swiergiel,[3] and François Hild[2]**

Abstract

This paper discusses the dual use of digital image correlation (DIC) and thermoelastic stress analyses (TSA) for the study of propagating cracks. It is shown that a few critical parameters such as emissivity and the thermoelastic constant, required for the latter can be calibrated with the former. A unified framework is introduced, which treats both experimental techniques equally to locate crack tips, and then evaluate stress intensity factors. This framework allows for a detailed quantitative comparison between both methods. It is found that, for the case at hand, the TSA outputs were less noise sensitive while the DIC method was less dependent on calibration. The proposed procedure was very robust for finding the crack tip location for both experimental methods.

Keywords

Crack tip position; Stress intensity factor; Thermoelastic coupling; Williams' series.

Introduction

The development of aircrafts and launch vehicles requires their integrity to be assessed as best as possible. One of the critical aspects is related to the presence of cracks. Some of them may propagate under static load and/or repeated cycles. Standards have been proposed to gather fatigue crack growth data, in particular for 'evaluating isotropic metallic materials under predominantly linear-elastic stress conditions and with force applied only perpendicular to the crack plane (mode I stress condition), and with a constant force ratio'[1]. In such approaches, the stress intensity factor (SIF) amplitude and crack length have to be determined as accurately as possible during the whole experiment.

Among the various techniques used to evaluate fracture mechanics parameters, full-field measurements are appealing since they rely on very large numbers of measurement points with modern acquisition devices (*e.g.,* visible light and IR cameras). Thermoelastic stress analysis (TSA) is one of such approaches[2–4], which uses the thermoelastic coupling to evaluate stresses from temperature measurements. One critical aspect of the technique is related to its careful calibration[5–7].

One area of application that is of particular interest consists in monitoring propagating cracks via TSA[8]. SIF and T-stress amplitudes were determined by post-processing measured temperature fields, provided the crack tip location was determined. One conventional way is to consider the so-called thermoelastic phase[7,9–11]. It is interesting to note that most of the time, line data are utilized to determine SIF amplitudes[8,11] or a limited number of data points[7,12].

[1]Département de Génie Mécanique (DGM)
ENS Paris-Saclay/CNRS/Université Paris-Saclay, Cachan, France
[2]Laboratoire de Mécanique et Technologie (LMT)
ENS Paris-Saclay/CNRS/Université Paris-Saclay, Cachan, France
[3]Formerly at Airbus Group Innovations, Suresnes, France
now at ArianeGroup, Les Mureaux, France

Corresponding author:
François Hild. Laboratoire de Mécanique et Technologie (LMT)
ENS Paris-Saclay/CNRS/Université Paris-Saclay
61 avenue du Président Wilson, 94235 Cachan, France
Email: francois.hild@ens-paris-saclay.fr

Another approach to the study of propagating cracks is via digital image correlation (DIC). DIC was used to evaluate SIFs since its early developments under dynamic and quasi static loading conditions[13–15]. More recently, fatigue crack propagation was studied via integrated approaches[16,17]. Such DIC techniques are based upon the use of Williams' series[18] (*i.e.,* the 2D elasticity solution to cracked media[19]) in registration algorithms[20].

IR Thermography (IRT) has also been combined with DIC. For instance, Chrysochoos et al.[21] showed a combined application of DIC and IRT in fatigue of a dual phase steel. Qualitative comparisons between TSA signals and strain fields were performed by Backman et al.[22], and damage was analyzed in fiber reinforced polymers[23]. In some instances, the dual use of DIC and IRT allowed Lagrangian temperature fields to be measured[24,25]. In all afore-mentioned cases, opposite faces were imaged for DIC and IRT purposes. The use of a dichroic mirror enabled Bodelot et al.[26] to perform simultaneous kinematic and thermal measurements on the same face of a stainless steel sample. An alternative route is to perform DIC analyses by registering IR frames[27,28]. Either pre-filtering of images[28] or brightness corrections accounting for temperature variations[27] were implemented to measure Lagrangian temperature fields. Very recently, hybrid techniques were introduced to extend such measurements to multiview analyses[29,30].

TSA (and DIC) generally subdivide the analyses into two steps for each time increment, (*i*) find the crack tip location, (*ii*) find the SIFs and related parameters such as T-stress. Most studies[8–12] apply distinctly different techniques for the two steps; some include the position of the crack tip in the minimization scheme evaluating SIFs[7,31]. For the first step, a wide range of propositions is found. For the second step, typically an analytical model (*e.g.,* Williams' series) of the observable (*i.e.,* displacement, temperature) is fitted to a special selection of data points. Since this closed-form solution is highly dependent on the crack tip position, there is a strong interplay between the two steps. Additionally, the data are noisy, and using the maximum number of data points is advantageous with respect to noise attenuation. The above mentioned integrated DIC method[16,17] has two advantages, namely (*i*) it uses a crack tip locating method

consistent with the analytical model used in step 2, (*ii*) it uses all available data points within a circular region of interest centered about the crack tip.

In the present work, the key features of integrated DIC[16,32] are also adopted for TSA data. The *same* Williams' series is used for both locating the crack tip *and* obtaining the SIFs and T-stress. The only change is that the Williams' series is written in terms of the stress tensor trace instead of displacements. This is akin to what is often found in TSA literature[7–12] except with the possibility of using more than just the first singular term. In particular, the first supersingular field is of special interest as its amplitude should cancel out if the crack tip is correctly located[32–34]. This approach thus provides a means of locating crack tips using a consistent definition with the other terms of Williams' series.

A Center Crack Tension (CCT) experiment is performed when prepared to simultaneously acquire DIC data on one sample face and TSA data on the other one. It allows for a direct comparison of the unified method on the two highly distinct data sets. The paper is organized as follows. First, the procedure for locating the crack tip with displacement and stress-based Williams' series is introduced. Second, the experimental protocol is presented for the fatigue test that is analyzed herein. Third, the results obtained by integrated DIC and TSA are discussed. In particular, the calibration of the latter by the former is studied. The crack tip positions and SIF amplitudes are compared when the *same* physical region is used in both approaches.

Crack tip location with Williams' series

The location of the crack tip is an experimental challenge when global fracture mechanics parameters are to be estimated[32]. Further, the concept of crack tip *itself* is related to models (*e.g.,* linear elastic fracture mechanics[19]). In DIC, the classical way is to minimize the displacement residuals between measured and theoretical fields[14] for different crack tip positions[20]. An alternative route is provided by considering Williams' displacement fields $\boldsymbol{\varphi}_n^I$ and $\boldsymbol{\varphi}_n^{II}$ of an infinite

medium containing a semi infinite crack along the x-axis ($x \leq 0$)

$$\mathbf{u}(\mathbf{z}) = \sum_{j=I}^{II} \sum_{n=n_{\min}}^{n_{\max}} a_n^j \boldsymbol{\varphi}_n^j(\mathbf{z}) \tag{1}$$

with

$$\begin{aligned} \boldsymbol{\varphi}_n^I(r,\theta) &= \tfrac{A(n)}{2\mu\sqrt{2\pi}} r^{n/2} \left[\kappa \exp\left(\tfrac{in}{2}\theta\right)\right. \\ &- \tfrac{n}{2} \exp\left(\tfrac{i(4-n)}{2}\theta\right) \\ &+ \left.\left((-1)^n + \tfrac{n}{2}\right) \exp\left(-\tfrac{in}{2}\theta\right)\right] \end{aligned} \tag{2}$$

$$\begin{aligned} \boldsymbol{\varphi}_n^{II}(r,\theta) &= \tfrac{iA(n)}{2\mu\sqrt{2\pi}} r^{n/2} \left[\kappa \exp\left(\tfrac{in}{2}\theta\right)\right. \\ &+ \tfrac{n}{2} \exp\left(\tfrac{i(4-n)}{2}\theta\right) \\ &+ \left.\left((-1)^n - \tfrac{n}{2}\right) \exp\left(-\tfrac{in}{2}\theta\right)\right] \end{aligned} \tag{3}$$

and

$$A(n) = \cos\left(\frac{n\pi}{2}\right)^2 + \sin\left(\frac{n\pi}{2}\right) \tag{4}$$

where (r,θ) are the polar coordinates with respect to the crack tip location, $\mathbf{z} = r\exp(i\theta)$ the affix of any point, μ Lamé's modulus, and $\kappa = (3-\nu)/(1+\nu)$ Kolossov's constant under plane stress assumption (ν denotes the Poisson's ratio of the considered material). The truncation orders $n_{\min}$ and $n_{\max}$ will be discussed in the sequel.

These mode I and II displacement fields have finite strain energies when their order $n \geq 0$. When $n = 1$, the corresponding fields are the standard mode I and II contributions whose amplitudes a_1^j are proportional to the SIFs. Conversely, when $n = 2$ and $j = I$, the amplitude a_2^I is proportional to the T-stress. Higher order (*i.e.,* subsingular) terms allow the effect of boundary conditions to be captured. Supersingular terms (*i.e.,* when $n < 0$) are usually discarded as they would induce diverging strain energies at the crack tip. However, it was shown that the first supersingular fields ($n = -1$) could be used to position the crack tip by canceling out the corresponding amplitudes[16,33,34]. Further, even in the presence of nonlinear phenomena in the vicinity of the crack tip, it was shown that the first supersingular term could be used to precisely pinpoint the crack tip; the third of these fields enabled the size of the process zone to be to evaluated[33,34].

Integrated DIC then consists in directly implementing the previous fields in the registration procedure[20]. The output of integrated DIC is the current set of unknown amplitudes $\tilde{a}_n^j$. Such computation is performed with an assumed crack tip position. The crack tip position is then updated by computing the crack tip offset[33]

$$\delta = -\frac{2\tilde{a}_{-1}^I}{\tilde{a}_1^I} \tag{5}$$

and an integrated DIC step is run again. When the absolute crack tip offset becomes less than 0.1 pixel, then the registrations are stopped.

The same approach is now developed to analyze Williams' series of the trace of the stress tensor $\boldsymbol{\sigma}$[18], which is used in TSA,

$$\mathrm{tr}(\boldsymbol{\sigma}(\mathbf{z})) = \sum_{j=I}^{II} \sum_{p=p_{\min}}^{p_{\max}} b_p^j \psi_p^j(\mathbf{z}) \tag{6}$$

with

$$\begin{aligned} \psi_p^I(r,\theta) &= 2p\ r^{p/2-1} \cos\left(\tfrac{(p-2)}{2}\theta\right) \\ \psi_p^{II}(r,\theta) &= 2p\ r^{p/2-1} \sin\left(\tfrac{(p-2)}{2}\theta\right) \end{aligned} \tag{7}$$

It is worth noting that the field ψ_2^{II} is vanishing and was not included in any of the following discussions. The truncation orders $p_{\min}$ and $p_{\max}$ will also be discussed later on.

As for displacement fields[32], the derivatives of the previous fields with respect to the crack tip position along the x-direction (*i.e.*, $-\partial\psi_p^j/\partial x$) still belong to the Williams' series

$$\frac{\partial \psi_p^j}{\partial x} = \frac{p}{2}\psi_{p-2}^j \tag{8}$$

It follows that when the crack tip is mispositioned by a small offset δ, the new stress decomposition is approximated, up to first order in δ, as

$$\mathrm{tr}(\boldsymbol{\sigma}(\mathbf{z}+\delta)) \approx \sum_{j=I}^{II} \sum_{p=p_{\min}}^{p_{\max}} \tilde{b}_p^j \left(\psi_p^j(\mathbf{z}) + \delta\frac{p}{2}\psi_{p-2}^j(\mathbf{z})\right) \tag{9}$$

where $\tilde{b}_p^j$ denote the amplitudes when $\delta \neq 0$. The latter ones are related to those for the exact solution (*i.e.*, $\delta = 0$) by

$$b_p^j = \tilde{b}_p^j + \frac{p+2}{2}\tilde{b}_{p+2}^j\delta \tag{10}$$

The crack tip is positioned in such a way that $b^I_{-1} = 0$ so that a first order estimate of the offset δ reads

$$\delta \approx -\frac{2\tilde{b}^I_{-1}}{\tilde{b}^I_1} \tag{11}$$

It is worth noting that the same derivation holds for the mode-II fields.

These results can be used for TSA. Under adiabatic assumptions, the thermoelastic coupling allows the amplitude of stress tensor trace to be related to the temperature amplitude ΔT[4]

$$\mathrm{tr}(\Delta\boldsymbol{\sigma}) = C\Delta T \tag{12}$$

with

$$C = \frac{\rho c_p}{\alpha T_0} \tag{13}$$

that defines the thermoelastic constant, which depends upon the coefficient of thermal expansion α, the heat capacity at constant pressure c_p, and the mass density ρ of the studied material. These expressions are valid provided the temperature variations are small in comparison with the initial temperature T_0, and when the variations of all thermophysical parameters with temperature are neglected.

From the measured temperature fields, TSA provides estimates of stress tensor trace fields by using Equation (12). With the Williams' series, see Equation (6), the corresponding amplitudes $\Delta\tilde{b}^j_p$ are determined via least squares fit for a given crack tip position. As for DIC, once the amplitudes are estimated, the new crack tip position can be updated by using Equation (11). When the absolute crack tip offset becomes less than 0.1 pixel, the iterative procedure is stopped.

Experimental Protocol

Sample preparation and camera calibration

The studied geometry was a center cracked tension (CCT) specimen (Figure 1(a)) made of 2024 aluminum alloy with the T351 heat treatment. This material is classically used in aeronautics and aerospace industries[35]. The sample size was $150 \times 50 \times 2$ mm (*i.e.,* a CCT50 geometry) with an 8 mm pre-notch machined via EDM from a 3-mm in diameter hole. One side of the sample was speckled with

black and white paints for DIC purposes (Figure 1(b)). Conversely, the other side was coated with a high emissivity (black) paint for IRT (Figure 1(c)). In the present case, the two cameras thus monitored *opposite* surfaces. Consequently, each of the selected technique used images that were considered "optimal" (*i.e.,* highly contrasted pattern for DIC purposes (Figure 1(b)), and uniform emissivity for IRT (Figure 1(c)).

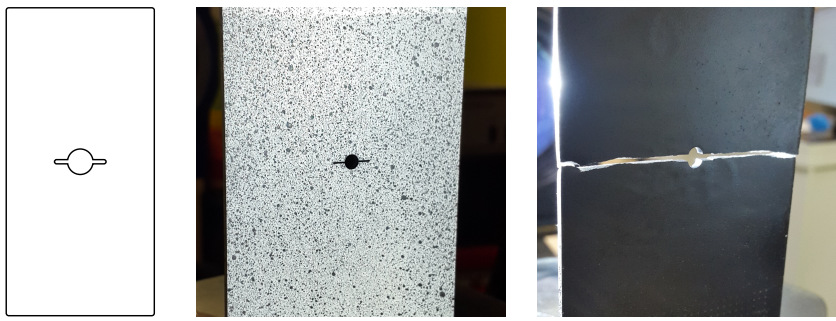

(a) (b) (c)

Figure 1. (a) Schematic view of the CCT geometry. (b) Speckled surface for DIC at the beginning of the test. (c) Matte surface for IRT at the end of the test.

When integrated DIC is to be performed with Williams' series (Equation (1)), there are three parameters that are required, namely, the Young's modulus of the material (here equal to 72 GPa), the Poisson's ratio (0.33), and the physical size of one pixel (*i.e.,* 50 µm). The latter was determined from the evaluation of the width of the sample in the picture in the reference configuration as observed by the visible light camera (Figure 1(b)) and then converted into metric units having measured the sample width.

For IRT, a calibration step is required to transform digital levels into temperatures (Table 1). A calibrated black body was used (Figure 2) in front of the IR camera. Twelve temperature increments were applied between 25 and 35°C. From these 12 images a quintic polynomial map was fitted for each pixel, which was later used to convert digital levels into temperature. With the selected objective lens, the physical size of one pixel was 171 µm. It was determined the same way as for the visible light camera.

Table 1. IR camera calibration

Black body	HGH DCN1000
NUC correction	pixel to pixel
Interpolant	quintic
Temperature noise-floor	0.02°C

Figure 2. Black body used for the calibration of the IR camera

Mechanical test

The mechanical test was performed on a servohydraulic testing machine in which the sample was fixed with hydraulic grips (Figure 3).

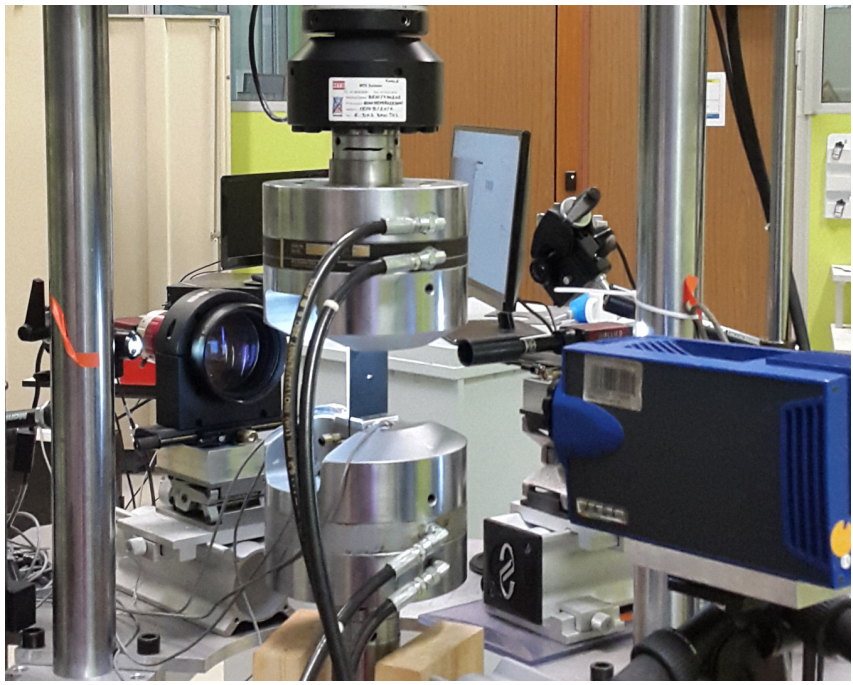

Figure 3. Experimental setup of the fatigue test

The hardware parameters of the optical setup are reported in Table 2 for the visible light and infrared cameras, which monitored opposite faces of the sample. It is worth noting that the camera definitions were significantly different. This point will be further commented in the sequel. Last, a telecentric lens was utilized to mitigate as much as possible any effect of out of plane motions on the DIC measurements.

Table 2. DIC and IRT hardware parameters

Visible light camera	Allied Vision Manta G-145B
Definition	1392×1040 pixels
Gray levels amplitude	8 bits
Telecentric lens	Edmund Optics $\times 0.125$
Field of view	70×52 mm^2
Image scale	50 µm/pixel
Stand-off distance	17 cm
Image acquisition rate	see text
Patterning technique	sprayed paints
Pattern feature size	10 pixels in diameter
IR camera	CEDIP Jade III MWIR (InSb)
Definition	240×320 pixels
Digital levels amplitude	14 bits
Lens	CEDIP MW 50-mm
Field of view	$11° \times 8°$
Image scale	171 µm/pixel
Stand-off distance	50 cm
Image acquisition rate	see text
Coating technique	sprayed black paint

During the whole test, the load history was controlled with a constant load ratio of 0.1. A series of 266 blocks of 1,000 cycles each was performed (Figure 4(a)). The first 33 blocks were carried at a maximum load of 8 kN to initiate a fatigue crack. The subsequent 133 blocks were performed at a maximum load of 4.5 kN. This level was selected since it was close to the propagation threshold of AA2024[35]. Last, 104 blocks were applied when the maximum load was increased to 6 kN. Each block consisted of 999 cycles performed at a frequency of 10 Hz (Figure 4(b)). The last cycle had constant levels to capture visible light pictures under stable conditions. During the first second of the each block, 100 IR pictures were acquired (at 100 Hz), capturing 10 cycles of each block.

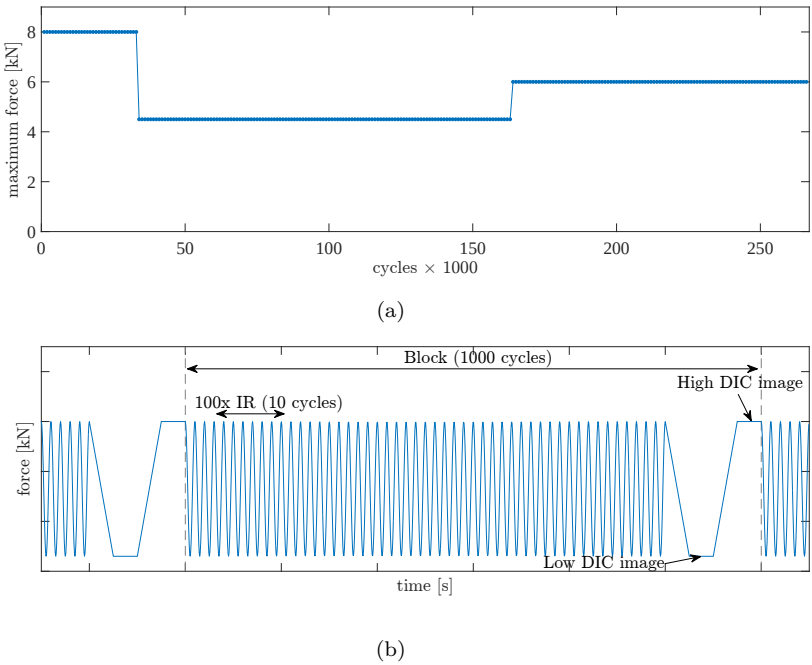

Figure 4. (a) Peak loading history of the fatigue experiment containing 266 blocks of each 1000 cycles. (b) Detail of one block, indicating the acquisition of 100 IR pictures and 2 visible light pictures.

DIC and TSA results

In the present analyses, regions of interest were considered with the *same physical* size. Two pacmen-like domains[36] were utilized with an outer radius of 10 mm, an inner radius of 1 mm to exclude the fracture process zone, and an additional mouth opening of 1 mm was applied to exclude the crack mouth from the analyses (Figure 5). Given the fact that the outer radius was chosen a priori, convergence analyses were required to study the dependence of the fracture mechanics parameters with the truncation orders (*i.e.*, $n_{\min}$ and $n_{\max}$, see Equation (1), as well as $p_{\min}$ and $p_{\max}$, see Equation (6)). The lower bounds $n_{\min}$ and $p_{\min}$ were set to -1 to include the first supersingular field that is used to locate the crack tip. No additional supersingular fields were considered. The choice of the upper bounds (*i.e.*, $n_{\max}$ and $p_{\max}$) is studied hereafter.

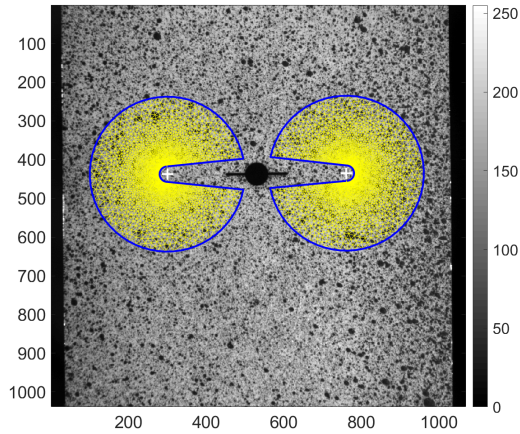

Figure 5. Pacmen-like regions of interest for integrated DIC and TSA. The crosses indicate the current crack tip positions. The (yellow) mesh made of 3-noded triangles is used in integrated DIC.

Choice of n_{max} for integrated DIC

Integrated DIC was run for the two tips of the fatigue crack. Each pacman, whose external radius is equal to 200 pixels, was then meshed with a density that varies with the radius (Figure 5). With such procedure, a finite element based DIC code dealing with 3-noded triangles (*i.e.,* T3-DIC[37]) could be used where each Williams' field appears as one mode that is projected onto the considered mesh. In all DIC analyses, the reference and deformed images were those for the same block (*i.e.,* what is sought are amplitudes of SIFs and T-stresses).

The crack path was determined by correlating the picture of the open crack of the last block with the initial picture with a standard T3-DIC code. From the gray level residuals, the crack path of both tips was obtained. Integrated DIC will then locate the tips to be positioned along this path by canceling out the amplitudes for the first mode I supersingular field as explained above.

Once all these parameters are set, the last choice is related to the number of terms to consider in Williams' series (Table 3). A convergence analysis is performed[36,38] to determine $n_{\max}$. The integrated DIC code is run on the whole set of pictures for $n_{\max}$

ranging from 3 to 23. In the present case, the reference solution is selected as that when $n_{\max} = 23$.

Table 3. Integrated DIC analysis parameters

DIC software	Correli 3.0[36,39]
Image filtering	none
Kinematic basis	truncated Williams' series
Region of interest	see Figure 5
Matching criterion	sum of squared differences
Interpolant	cubic
Parameter noise-floor	see text

Figure 6 shows the root mean square difference between the reference solution and the results for lower numbers of fields. As $n_{\max}$ increases, the truncation error decreases, which is expected[36,38]. Convergence is achieved when the RMS difference becomes lower than the standard uncertainties determined for the second phase of the loading history (Figure 4(a)) when $n_{\max} = 23$ (*i.e.,* 250 µm or 5 pixels for the crack tip position, 0.25 MPa$\sqrt{\text{m}}$ for the SIF amplitude, and 4 MPa for the T-stress amplitude). It is worth noting that these levels include all sources of experimental uncertainties related to the DIC technique, the camera *and* the feedback loop of the testing machine. The convergence is faster for the crack tip position ($n_{\max} > 3$) than the SIF amplitude ($n_{\max} \geq 9$), itself faster than the T-stress amplitude ($n_{\max} > 17$). As the main focus on the following analyses is related to the crack length and SIF amplitudes, the choice $n_{\max} = 9$ is made.

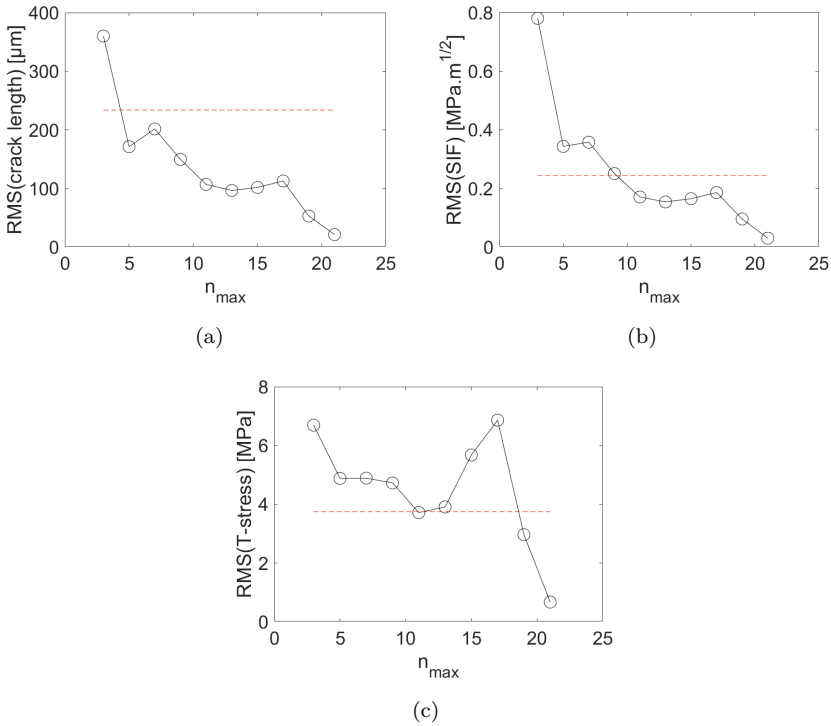

Figure 6. RMS differences of the crack length (a), mode I SIF amplitude (b), T-stress amplitude (c) for different truncation levels $n_{\max}$ with respect to the reference solution ($n_{\max} = 23$). The dashed lines depict the standard uncertainties when $n_{\max} = 23$.

Calibration of TSA with DIC

Before starting TSA, the first question to address was whether kinematic compensation[24,25] was needed. Figure 7 shows the history of rigid body translations for the whole specimen as evaluated with integrated DIC (*i.e.,* with the $\boldsymbol{\varphi}_0^j$ fields). During virtually all the test, the rigid body translation amplitudes were lower than 10 µm (*i.e.,* 0.2 pixel for the visible light camera and 0.06 pixel for the IR camera). Consequently, no kinematic compensation was performed on the temperature fields.

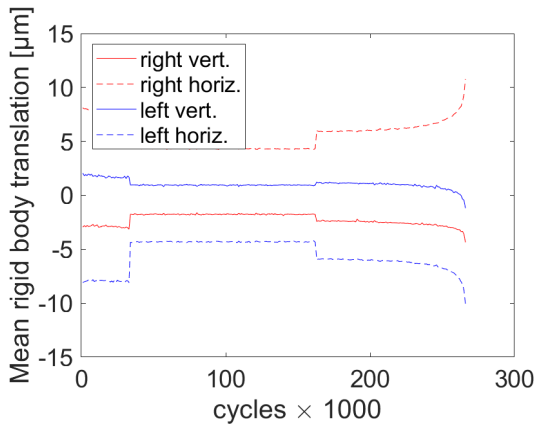

Figure 7. Rigid body translations of the two pacmen evaluated via integrated DIC

In the following analyses, the physical size of the pacmen are identical to those used for integrated DIC analyses (*e.g.*, the external radius is equal to 10 mm or 59 pixels for the selected resolution of the IR camera). The first step of TSA is to obtain the amplitudes of the temperature field for the 100 IR frames that are acquired for each block of cycles (Figure 4(b)). The amplitude field is obtained by keeping only the 10 Hz component via Fourier transform[24,28]. Figure 8 shows the amplitude field for the 166^{th} block.

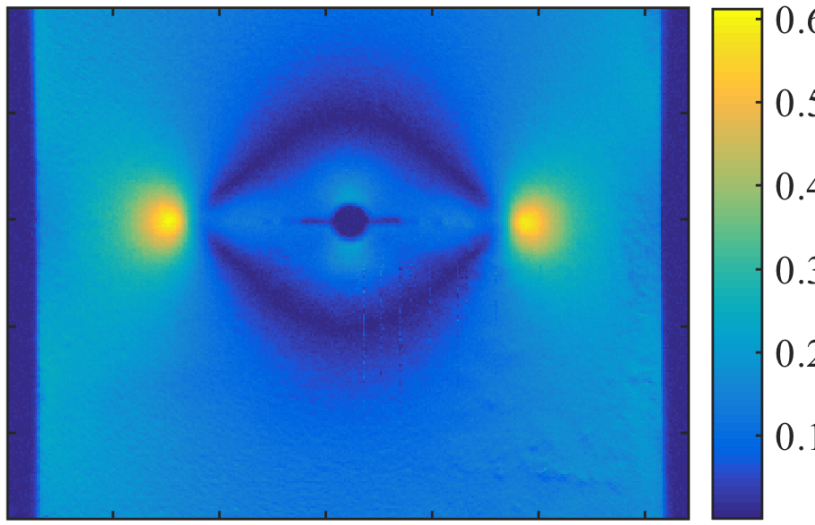

Figure 8. Temperature amplitude field expressed in K.

As for integrated DIC[36,38], the choice of the truncation of Williams' series has to be addressed. Only the values of $p_{\max} = [1, 2, 3]$ allowed for convergence while also determining the crack tip position. Locating the crack tip is essential, which limits the available terms in Williams' series for TSA. However, it is possible to locate the crack tip using a low value for $p_{\max}$ in the first pass and subsequently set the crack tip while increasing $p_{\max}$ in the second pass.

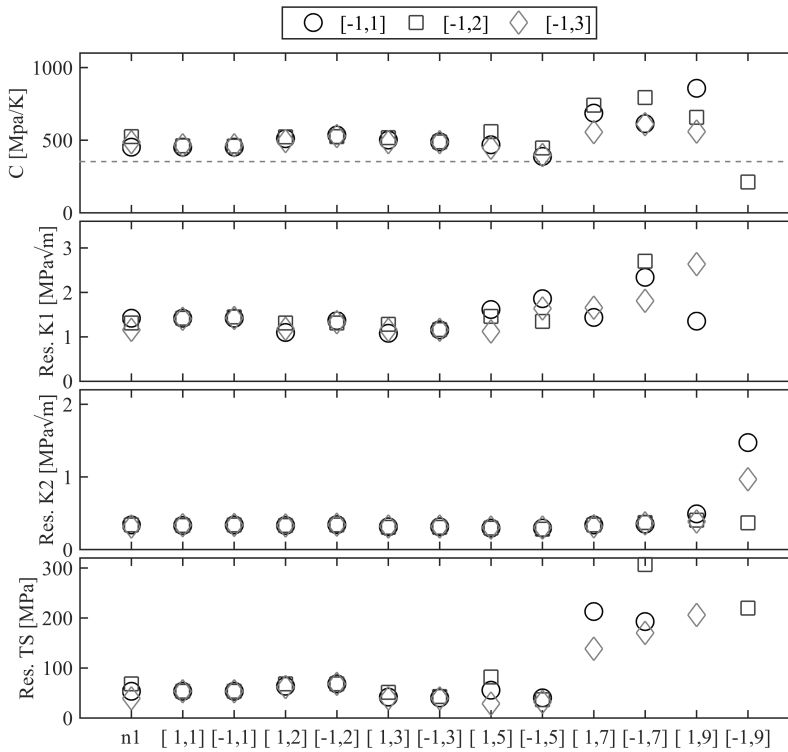

Figure 9. (Top row) The TSA thermoelastic constant as obtained by calibration using the integrated DIC mode I SIF (ΔK_I) for the first pass (first column) and the two-pass analyses starting from each of the three first-pass results (subsequent columns), where the brackets indicate the lower and upper truncation levels $[p_{\min}, p_{\max}]$. (Rows 2-4) RMS residuals between the mode I SIF, mode II SIF and the T-stress for the respective one-pass and two-pass analyses.

To determine how many terms are optimal, the TSA results for both SIFs and T-stress are compared to those obtained by DIC after fitting the thermoelastic constant C using as reference the ΔK_I data obtained via integrated DIC. Figure 9 shows the RMS residuals, for the first pass $p_{\max} = [1, 2, 3]$, in the first column indicated pass 1 as well as the results, for the second pass $p_{\max} = [1, \ldots, 9]$, when using the crack tip locations as determined by each first pass. Each second pass is indicated with its $[p_{\min}, p_{\max}]$ truncation below the figure. Additionally, this figure shows the thermoelastic constant C that was applied to minimize this residual.

The following observations can be made:

- The residual in SIF between both methods is slightly above 1 MPa$\sqrt{\text{m}}$, which is about 10% of the SIF range as will be shown below. This result shows that both methods are in reasonable agreement with each other.
- The T-Stress residuals are of the order of 80 MPa for $p_{\max} < 5$. This residual is very high (*i.e.,* about 100 % of the level obtained by integrated DIC). This observation indicates that the signal for the corresponding (TSA) Williams' term was too weak and measurements of the T-Stress by TSA are unreliable for this experiment.
- All results for $p_{\max} \leq 5$ show comparable residuals. This trend shows that there is no significant improvement obtained when adding higher order terms.
- All results for $p_{\max} > 5$ show diverging estimates, thereby indicating that the method has lost its conditioning for this experiment. Other experiments with higher resolution cameras may presumably allow these higher order terms to be captured.
- The calibrated thermoelastic constant C for $p_{\max} \leq 5$ is generally higher than that estimated using material parameters found in the literature (*e.g.,* 350 MPa/K when $c_p = 870$ J/kg/K, $\alpha = 23 \times 10^{-6}$ K^{-1}, and $\rho = 2780$ kg/m^3). This is partly due to the fact that the sample emissivity was different from the black body emissivity. However, this difference confirms that the calibration of TSA is critical[5–7] and should be performed for each experiment.

It is concluded that the two-pass analysis is not needed and that pass 1 with $p_{\max} = 3$ yields one of the best results. For that case, the calibration error is equal to 1 MPa$\sqrt{\text{m}}$, which is comparable to the standard uncertainty, which was estimated from the mode II SIF residuals. In the present case, the residuals on the T-stress amplitudes via TSA indicate that they are not trustworthy.

Final results and discussion

Figure 10 shows the crack lengths when estimated by integrated DIC and TSA. Even though the analyses were not performed on the same side, there is a clear correlation between both approaches.

The standard uncertainties evaluated for the second step of the experiment are equal to 190 µm for integrated DIC and 35 µm for TSA. This difference can be understood by the fact that TSA uses $59^2\pi \times 100 \approx 1.1$ Mpixel for the evaluation of the temperature amplitudes as opposed to $200^2\pi \approx 0.1$ Mpixel for integrated DIC. This order of magnitude difference has a direct effect on the measurement uncertainties.

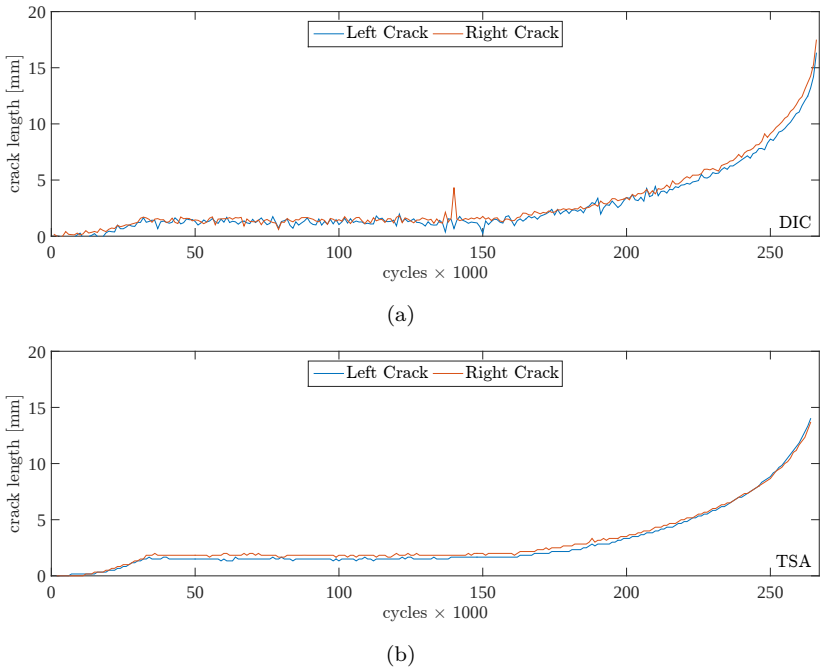

Figure 10. Crack lengths for the left and right tips determined via integrated DIC (a) and TSA (b)

The SIF amplitudes in modes I and II evaluated via integrated DIC and TSA are shown in Figure 11. The overall trends are identical for both techniques. They both conclude that the experiment is essentially activating the mode I regime. The standard uncertainties on the mode II SIF amplitude are respectively equal to 0.18 MPa$\sqrt{\text{m}}$ and 0.04 MPa$\sqrt{\text{m}}$. The RMS difference between the mode I amplitudes is of the order of 1 MPa$\sqrt{\text{m}}$. This level is higher than the measurement uncertainties of both methods. This result indicates

that there other sources of errors between the two methods (some of them related to the fact that the surfaces of interest are different).

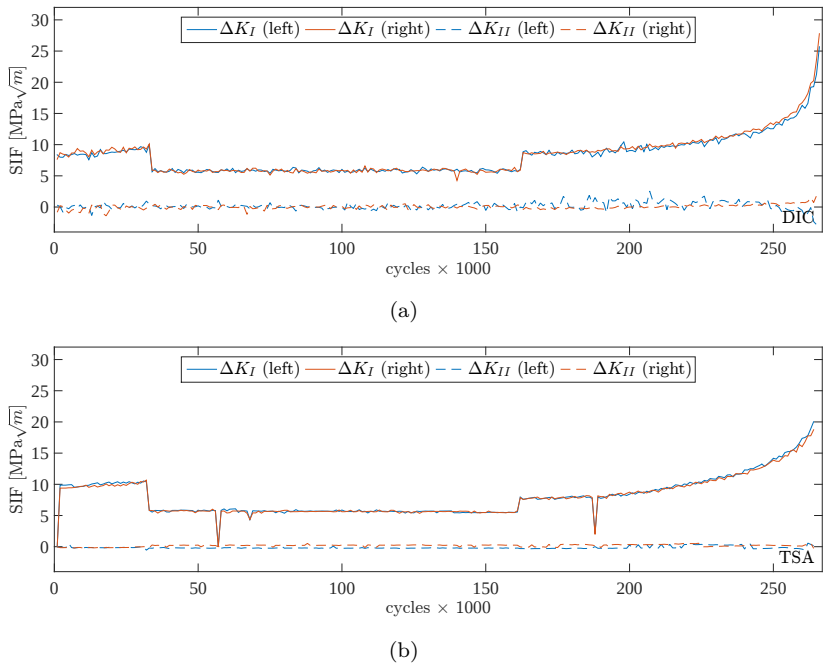

Figure 11. Mode I and II SIF amplitudes for the left and right cracks evaluated via integrated DIC (a) and TSA (b)

Figure 12 shows the global residuals of integrated DIC and TSA for all analyzed blocks. There is a clear difference between these quantities for integrated DIC and TSA. For integrated DIC, their overall levels being of the order of 1.5% of the dynamic range of the camera sensor, which are rather low, the results are deemed trustworthy. Further, the residual levels are virtually independent of the number of cycles, which indicates that the trustworthiness of the results is identical for the whole sequence and both crack tips. These results validate the choice of the pacmen geometry and the truncation bounds ($n_{\min}$ and $n_{\max}$) of Williams' series). From all these trends, it is concluded that the calibration of TSA via DIC analyses can be performed. Conversely, the TSA residuals have a variation that are similar to the mode I SIF history. This observation indicates that there still remains a model

error that was not accounted for (*e.g.,* kinematic compensation, non linear phenomena in the process zone, heat conduction).

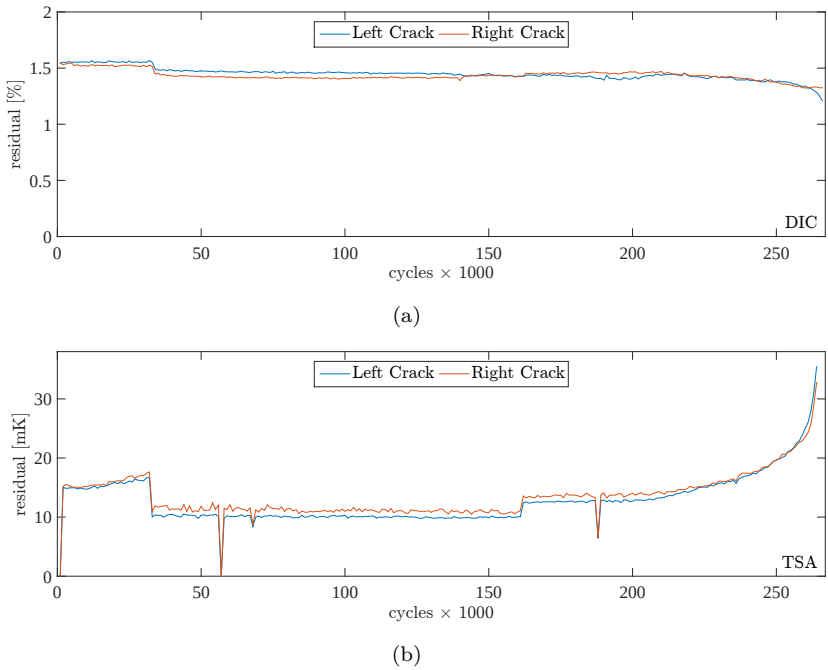

Figure 12. Residuals for the left and right cracks analyzed via integrated DIC (a) and TSA (b)

Conclusion and Perspectives

A unified framework to study propagating cracks via TSA and integrated DIC was proposed. It is based on the methodology previously applied in Integrated DIC using Williams' series, which were in the present work extended to be applicable to IRT data. This framework has two main advantages, irrespective of DIC or TSA:

- The location of the crack tip was determined by minimizing the amplitude of the first supersingular term. The main advantage is that by doing so, the definition of the crack tip location is consistent with the underlying fracture mechanics model as defined by Williams' series.

- The freedom to apply more than the classical 1st order term of Williams' series allows the model of the representation of the field surrounding the crack tip to be valid over a larger domain. Consequently, many more data points can be included in the analyses, typically, using a circular domain surrounding the crack tip. This greatly reduces the sensitivity to noise.

Using this unified framework, the mode I and II SIF amplitudes could be assessed when analyzing a fatigue test carried out on a CCT sample made of AA2024.

When using Williams' series, be they expressed in terms of displacements or stress trace, a convergence analysis is needed to select their truncation. In the present cases, pacmen-like domains were considered with the same physical size for both methods. About 10,000 IR pixels were considered herein for TSA as opposed to a limited number of evaluation points (*i.e.,* typically a few hundreds[7,8,12]). For integrated DIC, a very fast convergence was observed for the crack tip location, followed by the SIF amplitudes and then the T-stress amplitude. The maximum order could be increased at will without jeopardizing the overall convergence of the registration scheme. Such trend was not obtained for the TSA results reported herein. Only a limited number of terms allowed convergence to be achieved. This trend is due to the fact that the fields allowing the crack tip to be located and the SIF amplitudes to be estimated have a limited sensitivity.

One critical step of TSA is the calibration of the thermoelastic constant. In the present case, it was proposed to use integrated DIC, namely, the mode I SIF amplitude histories were considered and the minimization of the sum of squared differences enabled the thermoelastic constant to be tuned. The present procedure is different from what was proposed in the literature[5–7]. The calibration residuals were shown to be sufficiently low to deem integrated DIC and TSA trustworthy. Additional comparisons in terms of crack tip locations confirmed this conclusion. Further, the order of magnitude of the thermoelastic constant was found to be consistent, yet not identical, with literature data of AA2024-T351. This observation shows that calibration should be performed whenever possible.

The unified framework also allowed for a quantitative comparison of the two methods when using the same experiment, the same underlying theory, and the same physical size of the region of interest (*i.e.,* pacmen). It was shown that the thermoelastic constant as obtained using material parameters from the literature was unreliable, thereby giving a significant advantage to integrated DIC, which does not rely on that constant. However, ignoring this systematic error, the TSA results were shown to have measurement uncertainties significantly smaller. It should be noted that these results are not general to DIC or TSA, but are dependent on a plethora of choices made for this particular experiment (*e.g.,* the number of data points used in TSA was more than one order of magnitude higher than those available in integrated DIC). However, it is shown that TSA is a precise method.

The TSA outputs proved to be less noise sensitive. Yet, the DIC data were less reliant on calibration parameters such as emissivity and the thermoelastic constant and thus (for this case) more accurate. Since both methods are based on the same framework, the natural progression is to combine both methods to have the best of both worlds.

Acknowledgements

The studied sample was kindly provided by Airbus Group Innovations (Suresnes, France).

References

1. *ISO 12108:2018(en): Metallic materials – Fatigue testing – Fatigue crack growth method*. Geneva (Switzerland): International Organization for Standardization, 2018.
2. Stanley P and Chan W. Quantitative stress analysis by means of the thermoelastic effect. *J Strain Analysis* 1985; 20(3): 129–137.
3. Dulieu-Barton J and Stanley P. Development and applications of thermoelastic stress analysis. *J Strain Analysis* 1998; 33(2): 93–104.
4. Pitarresi G and Patterson EA. A review of the general theory of thermoelastic stress analysis. *J Strain Analysis* 2003; 38(5): 405–417.
5. Dulieu-Smith J. Alternative calibration techniques for quantitative thermoelastic stress analysis. *Strain* 1995; 31(1): 9–16.
6. Ju SH and Rowlands RE. Thermoelastic determination of ki and kii in an orthotropic graphite-epoxy composite. *J Compos Mat* 2003; 37(22): 2011–2025.

7. Díaz F, Yates J and Patterson E. Some improvements in the analysis of fatigue cracks using thermoelasticity. *Int J Fat* 2004; 26(4): 365–376.
8. Tomlinson RA and Olden EJ. Thermoelasticity for the analysis of crack tip stress fields — a review. *Strain* 1999; 35(2): 49–55.
9. Zanganeh M, Tomlinson RA and Yates JR. T-stress determination using thermoelastic stress analysis. *J Strain Analysis* 2008; 43(6): 529–537.
10. Patki AS and Patterson EA. Thermoelastic stress analysis of fatigue cracks subject to overloads. *Fat & Fract Eng Mat & Struct* 2010; 33(12): 809–821.
11. Ancona F, Palumbo D, Finis RD et al. Automatic procedure for evaluating the paris law of martensitic and austenitic stainless steels by means of thermal methods. *Eng Fract Mech* 2016; 163: 206–219.
12. Chen D, Sun S, Dulieu-Barton J et al. Crack growth analysis in welded and non-welded t-joints based on lock-in digital image correlation and thermoelastic stress analysis. *Int J Fat* 2018; 110: 172–185.
13. Peters W, Ranson W, Kalthoff J et al. A study of dynamic near-crack-tip fracture parameters by digital image analysis. *J Phys Coll* 1985; 46(C5): 631–638.
14. McNeill S, Peters W and Sutton M. Estimation of stress intensity factor by digital image correlation. *Eng Fract Mech* 1987; 28(1): 101–112.
15. Sutton M, McNeill S, Helm J et al. *Advances in Two-Dimensional and Three-Dimensional Computer Vision*, volume Topics in Appl. Phys., 77. Berlin (Germany): Springer, 2000. pp. 323–372.
16. Mathieu F, Hild F and Roux S. Identification of a crack propagation law by digital image correlation. *Int J Fat* 2012; 36: 146–154.
17. Mathieu F, Hild F and Roux S. Image-based identification procedure of a crack propagation law. *Eng Fract Mech* 2013; 103: 48–59.
18. Williams M. On the stress distribution at the base of a stationary crack. *ASME J Appl Mech* 1957; 24: 109–114.
19. Kanninen M and Popelar C. *Advanced Fracture Mechanics*. Oxford (UK): Oxford University Press, 1985.
20. Roux S and Hild F. Stress intensity factor measurements from digital image correlation: post-processing and integrated approaches. *Int J Fract* 2006; 140(1-4): 141–157.
21. Chrysochoos A, Berthel B, Latourte F et al. Local energy analysis of high-cycle fatigue using digital image correlation and infrared thermography. *J Strain Analysis* 2008; 43(6): 411–422.
22. Backman D, Cowal C and Patterson EA. Analysis of the effects of cold expansion of holes using thermoelasticity and image correlation. *Fat & Fract Eng Mat & Struct* 2010; 33(12): 859–870.
23. Battams G and Dulieu-Barton J. Data-rich characterisation of damage propagation in composite materials. *Compos Part A* 2016; 91: 420–435.
24. Silva ML and Ravichandran G. Stress field evolution under mechanically simulated hull slamming conditions. *Exp Mech* 2012; 52(1): 107–116.
25. Wang W, Fruehmann RK and Dulieu-Barton JM. Application of digital image correlation to address complex motions in thermoelastic stress analysis. *Strain* 2015;

51(5): 405–418.
26. Bodelot L, Sabatier L, Charkaluk E et al. Experimental setup for fully coupled kinematic and thermal measurements at the microstructure scale of an aisi 316l steel. *Mat Sci Eng* 2009; A501(1-2): 52–60.
27. Maynadier A, Poncelet M, Lavernhe-Taillard K et al. One-shot measurement of thermal *and* kinematic fields: Infra-red image correlation (iric). *Exp Mech* 2011; 52(3): 241–255.
28. Silva ML and Ravichandran G. Combined thermoelastic stress analysis and digital image correlation with a single infrared camera. *J Strain Analysis* 2011; 46(8): 783–793.
29. Charbal A, Dufour JE, Hild F et al. Hybrid stereocorrelation using infrared and visible light cameras. *Exp Mech* 2016; 56: 845–860.
30. Wang Y, Charbal A, Dufour JE et al. Hybrid multiview correlation for measuring and monitoring thermomechanical fatigue test. *Exp Mech* 2019; (DOI: 10.1007/s11340-019-00500-8).
31. Díaz F, Patterson EA, Tomlinson RA et al. Measuring stress intensity factors during fatigue crack growth using thermoelasticity. *Fat Fract Eng Mat Struct* 2004; 27(7): 571–583.
32. Roux S, Réthoré J and Hild F. Digital image correlation and fracture: An advanced technique for estimating stress intensity factors of 2d and 3d cracks. *J Phys D: Appl Phys* 2009; 42: 214004.
33. Hamam R, Hild F and Roux S. Stress intensity factor gauging by digital image correlation: Application in cyclic fatigue. *Strain* 2007; 43: 181–192.
34. Henninger C, Roux S and Hild F. Enriched kinematic fields of cracked structures. *Int J Solids Struct* 2010; 47: 3305–3316.
35. Forth S, Wright C and Johnston W. *7075-T6 and 2024-T351 Aluminum Alloy Fatigue Crack Growth Rate Data*. Report TM-2005-213907, NASA Langley, VA (USA), 2005.
36. Vargas R, Neggers J, Canto R et al. Analysis of wedge splitting test on refractory castable via integrated DIC. *J Europ Ceram Soc* 2016; 36: 4309–4317.
37. Leclerc H, Périé J, Roux S et al. *Integrated digital image correlation for the identification of mechanical properties*, volume LNCS 5496. Berlin (Germany): Springer, 2009. pp. 161–171.
38. Grabois T, Neggers J, Ponson L et al. On the validation of integrated DIC with tapered double cantilever beam tests. *Eng Fract Mech* 2018; 191: 311–323.
39. Leclerc H, Neggers J, Mathieu F et al. *Correli 3.0*. IDDN.FR.001.520008.000.S.P.2015.000.31500, Agence pour la Protection des Programmes, Paris (France), 2015.